Subinertial Response of a Density-Driven Eastern Boundary Poleward Current to Wind Forcing

ÁLVARO PELIZ

Instituto de Investigação das Pescas e do Mar, Lisbon, Portugal

JESÚS DUBERT

Departamento de Física, Universidade de Aveiro, Aveiro, Portugal

DALE B. HAIDVOGEL

Institute of Marine and Coastal Sciences, Rutgers—The State University of New Jersey, New Brunswick, New Jersey

(Manuscript received 13 December 2001, in final form 20 February 2003)

ABSTRACT

A high-resolution primitive equation numerical model is used to generate a poleward flow along a meridionally oriented eastern boundary slope/shelf system by imposing an along-coast density gradient as the forcing mechanism. Wind forcing is applied to the resulting quasi-steady current system, and the subinertial response is analyzed. Parallel experiments with no slope-poleward flow are conducted for comparison. Moderately strong upwelling- and downwelling-favorable, week-to-month-scale wind events modify the poleward flow but do not significantly change the density-driven current structure at the slope. The alongshore transport within the slope region is reduced by 0.2–0.3 Sv (from 1.2 Sv, where Sv $\equiv 10^6$ m^3 s^{-1}), under the influence of either downwelling or upwelling winds. Independent of the wind direction, the density-driven poleward flow always remains surface intensified. Wind-driven shelf currents develop with a considerable degree of independence from the slope-poleward circulation. On the shelf, the density field is modified by cross-shelf buoyancy advection within the boundary layers and by strong vertical mixing. The presence of the poleward flow over the slope constitutes an important factor in the behavior of the bottom boundary layer at the shelf break and for the patterns of cross-slope circulation.

1. Introduction

Many processes have been suggested as potential contributors to the generation and maintenance of eastern boundary poleward currents (EPC). Local to the continental shelf, these processes include coastal trapped waves, wind-driven up/downwelling, and eddy form stress. On the larger scale, extracoastal, meridional variations in density are also a possible forcing mechanism. In this study, we consider the last of these possibilities.

In the midlatitude oceans, meridional density gradients in the surface layers (typically 0–600-m depth) exist and are balanced by geostrophic eastward surface-intensified flow. When this flow approaches a meridionally oriented coast, adjustment processes occur and poleward currents may be generated. The theoretical framework for this adjustment was initially developed by Pedlosky (1974) and extended by Huthnance (1984) with application to the Rockall slope current. Subsequent observational and modeling work (e.g., Smith et al. 1991; Weaver and Middleton 1989; Dubert 1998) has shown that the adjustment of meridional density gradients at the slope is important, particularly along midlatitude eastern boundaries. Among the most cited examples are the Leeuwin Current (west Australia), the Davidson Current (U.S. West Coast), and the Iberian Poleward Current (IPC). See Neshyba et al. (1989) for an early review of eastern boundary poleward flows.

The Iberian Poleward Current is known to be a winter circulation feature (e.g., Frouin et al. 1990), notable in its thermal signature at the surface, consisting of a warm tongue that spreads along the slope and that usually develops in autumn at the latitudes of the mid–western Iberia coast (Fig. 1). This warm tongue has been observed to extend along the southern Bay of Biscay far beyond the forcing zone (Pingree and Le Cann 1989). During the summer period, this zone is under the influence of strong upwelling-favorable winds (e.g., Isemer and Hasse 1987) and the IPC is often not clearly observed at the surface.

Corresponding author address: Álvaro Peliz, IPIMAR DAA, Av. Brasília, 1449-006, Lisbon, Portugal.
E-mail: apeliz@ipimar.pt

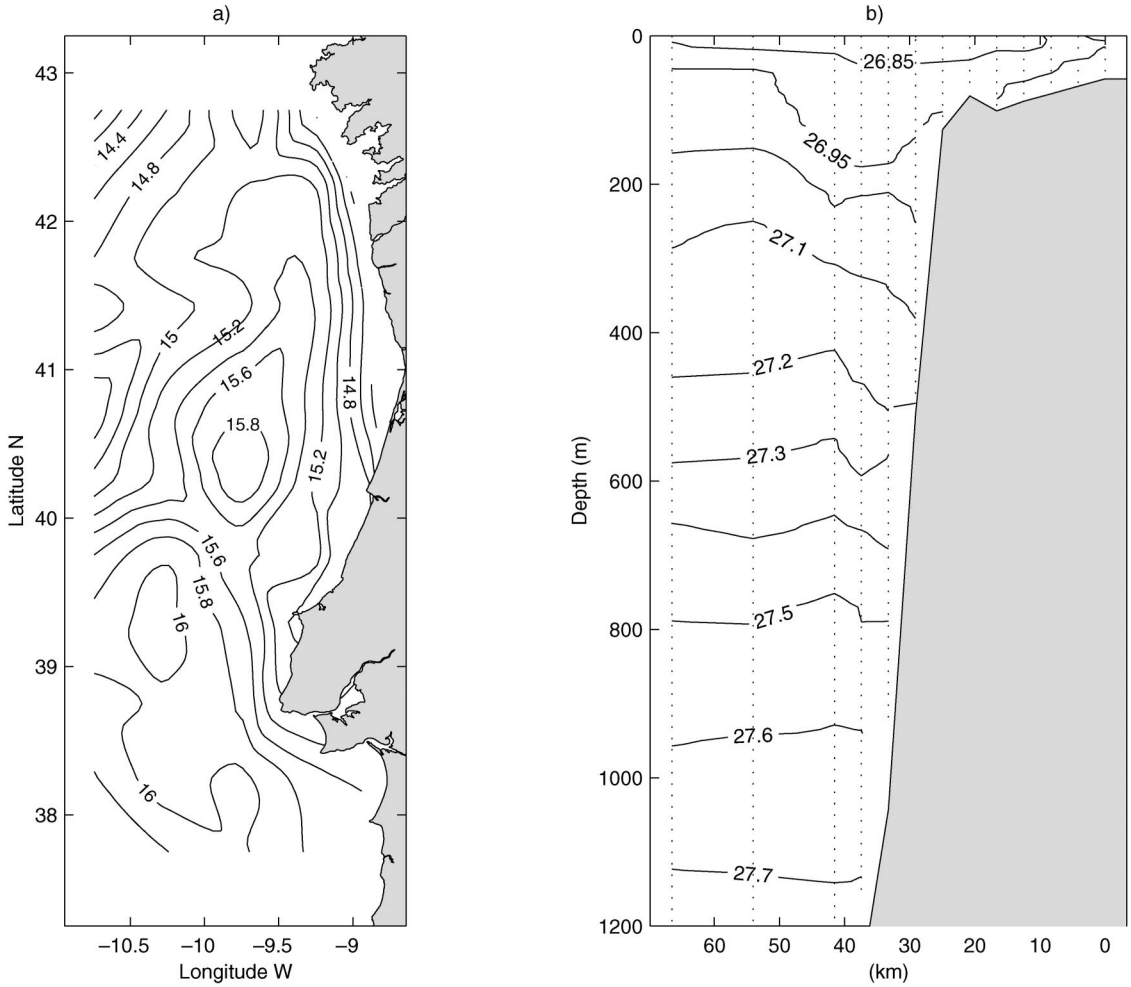

FIG. 1. Observations of the Iberian Poleward Current: (a) surface temperature field in Feb 1998 off western Iberia showing the IPC as a warm tongue narrowing northward (CTD data from the IPIMAR cruise 02020298); (b) a cross-slope section (41.6°N) of Feb 2000 showing the vertical density structure of the IPC during a coastal upwelling event (CTD data from the IPIMAR cruise 02040200).

Along the western coast of North America, a surface poleward flow along the slope is also observed during winter (Davidson Current). Here too there is strong seasonality, apparently related to variability of the local wind fields (e.g., Hickey 1998). In contrast, along the western coast of Australia equatorward winds prevail all year round. Nonetheless, slope-poleward flow is observed permanently although with variations in strength (e.g., Thompson 1987; Smith et al. 1991). In all these examples, the low-frequency poleward flow is (at least in part) density driven, and local wind forcing introduces variability in the coastal currents at seasonal and synoptic timescales.

In this work, mechanisms of subinertial variability of EPCs are explored. Our general objective is to investigate how the co-occurrence of meridional density gradients and alongshore wind stress modulate the circulation at the shelf and slope. Specifically, we seek to understand the influence of synoptic-scale wind forcing on an existing density-driven EPC. Questions addressed include: Is an upwelling-favorable wind event capable of reversing a density-driven EPC or pushing it to deeper levels? Does a downwelling wind significantly intensify the density-driven poleward flow at the slope? How different is the response of the cross-slope structure to wind forcing in the presence of a poleward slope current driven by meridional density gradients?

We assume below that the meridional density gradient is the primary factor driving the poleward slope flow. This assumption relies, in part, on the fact that at midlatitudes these gradients have scales of variability larger than those of the wind forcing. The simulations concentrate on events with timescales long enough to introduce significant changes in the shelf/slope system, but shorter than the variability of the large-scale density gradients themselves. A poleward flow is generated through a prescribed meridional density gradient, and the quasi steady state of the currents thus obtained con-

stitutes the initial state for the wind-forced simulations. The same forcing is applied to an initially resting, linearly stratified ocean in order to compare the response of the shelf/slope system with and without an active density-driven EPC.

To avoid the complex interaction of the poleward flow with rough bathymetry, a smooth shelf/slope system is used here. [However, see Peliz et al. (2003) for an investigation of such interactions.] The numerical study is inspired by the conditions of the Iberian Poleward Current. Considering the simplifications in the simulations, however, the results may have application to other EPC systems.

The next section describes the model and experimental configuration. In section 3, the adjustment of the meridional gradient and the generation of the poleward flow is described. In section 4, the density-driven poleward current is compared with some observations taken off Western Iberia. After a characterization of the wind forcing used, section 5 discusses the response of the system with and without slope-poleward flow to downwelling, upwelling, and variable wind forcing. Section 6 describes the results of sensitivity tests, and in the last section, the results are summarized.

2. Model and experimental configuration

The simulations described below were obtained with the Regional Ocean Modeling System (ROMS), a free-surface, hydrostatic, primitive equation ocean model that uses stretched, terrain-following coordinates in the vertical and orthogonal curvilinear coordinates in the horizontal. Although initially based on the *s*-coordinate model of Song and Haidvogel (1994), ROMS has recently been completely rewritten to improve both its numerics and efficiency in single and multithreaded computer architectures (Haidvogel et al. 2000). It has also been enhanced with new features including high-order, quasi-monotone advection schemes; accurate pressure gradient algorithms; a unified suite of air–sea–benthic boundary layers; and data assimilation capabilities. (A description of the ROMS model, as well as associated postprocessing software and an extensive suite of model test problems, is available online at ROMS Web site: http://marine.rutgers.edu/po/index.php.)

The model domain, meant to approximate the geometry of western Iberia, is a meridionally oriented mid-latitude channel bounded on the east by a continental slope and shelf as depicted in Fig. 2. The coordinate system is oriented as follows: *x* positive eastward *y* northward, and *z* upward. The bathymetry represents an idealized mid-Portugal continental margin depth profile. It is, however, kept uniform in the meridional direction, thus avoiding interaction of the poleward current with topographic irregularities (e.g., canyons, promontories, shelf width, and slope variations).

The model spans 9° of latitude (about 1000 km) and over 4° of longitude (about 340 km). The model resolution is fixed in the meridional direction (~4 km) and increases smoothly from the deep ocean (~6 km) toward the shelf (less than 2 km). Depths range from 1200 m in the far field to about 100 m at the shelf break and to a minimum depth of 23 m at the coast. The shelf is approximately 50 km in width. Sixteen vertical *s* levels are used. The stretching factors (Table 1) were selected in order to concentrate vertical resolution within the upper layers.

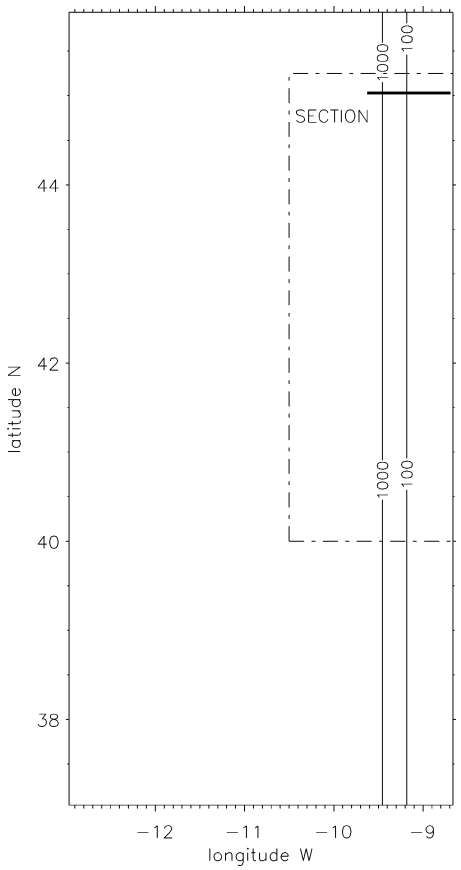

FIG. 2. Computational domain, with isobaths at 1000 and 100 m. The location of the vertical cross section referred to in the text is indicated by a thicker line crossing the slope at 45.0°N. The dashed box corresponds to the area of the horizontal fields plotted in Figs. 8 and 12.

The bathymetric profile was taken from a section at 41°N (see Fig. 1) and smoothed in order to minimize pressure gradient errors known to arise in terrain-following coordinates. Avoiding that source of error is especially important here, as the dynamics at the slope are the focus of the simulations. The resulting maximum *r* factor—a measure of likely error levels for sigma-coordinate models (e.g., Haidvogel and Beckman 1999)—is about 0.18. This is well below the empirical value (~0.3) above which large errors are known to arise in ROMS. A test with zero forcing conditions (with the density only varying vertically, $\partial\rho/\partial z = 0.86 \times 10^{-3}$

TABLE 1. Model parameters used in the central experiment.

L	97	No. of points in lon
M	258	No. of points in lat
N	16	No. of s levels
h_{max}	1200 m	Max depth of the domain
h_{min}	22.7 m	Min depth of the domain
θ_s	3.0	Sigma coordinate stretching factor
θ_b	0.2	Sigma coordinate bottom stretching factor
Δx	1.94–5.92 km	Resolution in the zonal direction
Δy	3.5–4.1 km	Resolution in the meridional direction
Δt	200 s	Baroclinic time step
Δt_f	6.67 s	Barotropic time step
ν	5.0 $m^2\ s^{-1}$	Laplacian horizontal viscosity
ν_t	5.0 $m^2\ s^{-1}$	Laplacian horizontal diffusivity
κ	$1.0 \times 10^{-5}\ m^2\ s^{-1}$	Vertical viscosity
κ_t	$0.5 \times 10^{-5}\ m^2\ s^{-1}$	Vertical diffusivity
r	$3.0 \times 10^{-4}\ m\ s^{-1}$	Linear bottom drag coefficient

kg m^{-4}) was performed and a maximum absolute velocity of about 0.5 cm s^{-1} was obtained after 10 days of simulation.

Open boundary conditions were used along the southern, western, and northern boundaries. Radiative conditions were used for all variables along with passive/active conditions for the tracer variables (Marchesiello et al. 1998). Inside a belt of six grid points along the north and west ends of the domain, relaxation toward reference values (e.g., Haidvogel et al. 1991) was used for tracers, free-surface elevation, and vertically integrated momentum. These reference values were calculated interactively in a first run where eventual disturbances at the boundaries were eliminated by extrapolating from the nearest unperturbed interior grid points. The timescale of the nudging was one day for passive/active conditions and 1–10 days (from the boundary points to the interior) for the interior relaxation. The bottom stress was parameterized using the linear relation $\tau_b = r v_b$ with, $r = 3 \times 10^{-4}$ m s^{-1} where v_b stands for the velocity at the deepest level. The vertical mixing scheme is based on the K-profile parameterization scheme developed by Large et al. (1994).

3. The initial quasi steady state (EPC)

The density forcing conditions are chosen to represent those of the IPC system and correspond to an idealization of the winter conditions observed by Mazé et al. (1997) in the French cruise ''Bord-Est 3'' of May 1989. These initial conditions were selected for several reasons. First, they correspond to one of only a few high-quality regional datasets. Second, an inverse model was used with these data to calculate budget estimates in the study area (Mazé et al. 1997). Third, they include observations taken sufficiently far from the coast to represent conditions to the west. The northward and vertically varying density field is given by

$$\sigma(y, z) = 26.9 - \frac{0.86z}{1000} - 0.1\left\{1 - \tanh\left[\left(-z - \left\{500 - 250\left[1 + \tanh\left(\frac{y - 400 \times 10^3}{200 \times 10^3}\right)\right]\right\}\right) \Big/ 100\right]\right\}. \quad (1)$$

Here y (latitude) and z (depth) are in meters. The background linear stratification ($26.9 - 0.86z/1000$) corresponds to a buoyancy frequency (N) of about 0.003 s^{-1}. The meridional variations in the stratification are shown in Fig. 3. (thin lines). The model is initialized with null velocity and a flat sea surface. At this stage, no atmospheric wind forcing is applied.

The adjustment of the meridional density gradient to the presence of the coastal margin proceeds as follows. [See also Dubert (1998) and Slørdal and Weber (1996).] The adjustment occurs in three stages with different timescales. In the first, fast Rossby adjustment of the free surface (initially flat) takes place. In the adjusted state (Fig. 4b), the offshore sea surface slopes down towards the north, thereby compensating at depth for the northward increase in baroclinic pressure, as required for a motionless deep ocean. An analytical example of this is provided in Middleton (2000). An accompanying geostropic shoreward flow of about 1–2 cm s^{-1} develops (Fig. 3, thicker lines), corresponding to a depth-integrated transport of approximately 1.2 Sv (Sv $\equiv 10^6\ m^3\ s^{-1}$).

The second stage of the adjustment corresponds to the interaction of the zonal flow with the shelf/slope topography. At the surface, away from the coast, the inflow is perpendicular to the density gradient and the isopycnals (Figs. 4a,b) remain perpendicular to the coast. However, near the slope a tonguelike structure in the density field develops and extends northward.

The generation and trapping of the current in the slope region may be explained using the vorticity equation of the depth-integrated linear steady-state flow (e.g., Mertz and Wright 1992):

$$\beta h \overline{v} = \frac{1}{\rho_0} J(P_b, h) + \mathrm{curl}_z(-\tau_b), \quad (2)$$

where ρ_0 is a reference density, β is the meridional variation of the Coriolis parameter, $\overline{v}$ is the depth-av-

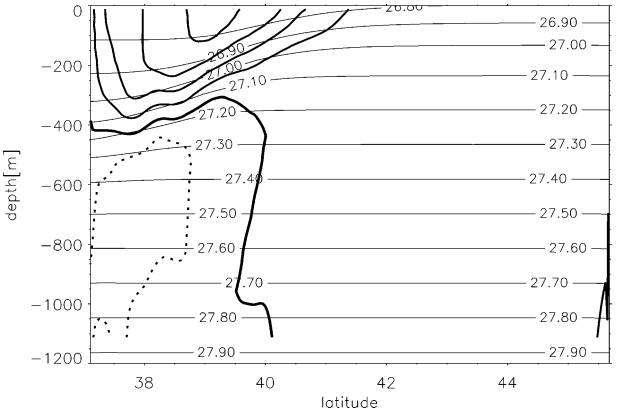

FIG. 3. The flow condition at the western edge of the domain. The density anomaly is represented with thinner lines. Thicker lines correspond to the adjusted eastward inflow at the initial state. Lines are plotted every 0.5 cm s^{-1} and dotted lines correspond to negative values. The flow is stronger at the surface with maximum values slightly above 2 cm s^{-1}.

eraged velocity (meridional component), h is the local depth, P_b is the bottom pressure, and τ_b is the bottom stress.

In view of the present configuration where h is meridionally uniform and disregarding the influence of the bottom stress, we simplify (2) to obtain

$$\rho_0 \beta h \overline{v} = -\frac{\partial P_b}{\partial y}\frac{\partial h}{\partial x}. \quad (3)$$

This equation expresses the balance of the planetary vorticity and the vortex tube stretching or bottom pressure torque (e.g., Holland 1973; Csanady 1988). In the vicinity of the slope $\partial P_b/\partial y > 0$ and $\partial h/\partial x < 0$, the northern heavier water tends to sink across the slope while southern lighter water tends to rise upslope generating a cyclonic torque responsible for the poleward flow (a poleward Sverdrup velocity).

Further understanding of the interaction of the zonal flow with the meridionally aligned slope may be obtained from considerations of potential vorticity conservation, as depicted in Fig. 5. The sketch represents the idealized response of a three-layer ocean adjacent to a continental margin. Following the setup of the onshore flow, the surface layer depth increases and gains cyclonic vorticity with the consequent generation of poleward flow. At the same time, layer 2 is compressed and gains anticyclonic vorticity. At this depth, the flow is equatorward.

The final stage of adjustment of the density gradient involves the propagation of the low-density tongue northward (Fig. 4a). As soon as the slope current is set up, the low density waters in the south begin to be advected poleward, generating a light water tongue that progresses along the slope on top of heavier northern waters.

The cross-shore structure of the resulting current system along the standard section (represented by the line crossing the shelf in Fig. 2) is plotted in Figs. 4c and 4d. The sections represent the vertical distribution of density and alongshore velocity at day 45 of the adjustment simulation. At the surface, a lens of light water has formed due to northward advection in the surface layers. In the interior, prominent downwelling of isopycnals is observed in the first 500 m (Fig. 4c). This tilt is related to the resultant poleward surface-intensified flow in the upper 300 m confined to the slope (~30 km wide) with values between 20 and 25 cm s^{-1} (Fig. 4d).

Below this upper layer, there is a weak undercurrent at about 600-m depth in agreement with the simple arguments above. With the poleward advection of the light water tongue, the cross-slope density gradients increase enhancing the vertical shear through thermal wind. By day 45, maximum equatorward velocities around 5 cm s^{-1} are observed at about 600-m depth (Fig. 4d). This undercurrent remains almost constant throughout the wind-forced simulations and is not discussed further.

Last, at the outer shelf, a surface countercurrent exists with a magnitude less than 5 cm s^{-1} (see shelf edge in Fig. 4d). This current is a result of the northward propagation of the light tongue. The inner side of the tongue corresponds to an upward tilt of the isopycnals with consequent generation of vertical shear through thermal wind and a surface-intensified equatorward flow is observed.

By day 45, the northern limit of the density tongue has left the domain by the northern boundary and an almost steady poleward flow structure is established. It was decided to use the results of day 45 as the initial conditions for the wind-forced simulations. This quasi steady state of the simulated EPC system will from now on be considered as day 0 of the simulations.

A comment on the persistence of the slope flow and the role of bottom dissipation is instructive. The timescale for frictional spindown in unstratified conditions is

$$T_f = H/r,$$

where H is the water depth and r is the drag coefficient. However, in stratified flows, the tendency of buoyancy effects to decouple the interior flow from the bottom boundary layer may become important, even in low-stratification conditions (Chapman 2002). This ''buoyancy shutdown'' process acts over a timescale (see Garrett et al. 1993):

$$T_b = \left(\frac{f}{\alpha N}\right)^3 \frac{U}{rN},$$

where U is a scale for the along isobath flow, α is the bottom slope, N is the buoyancy frequency, and f is the Coriolis parameter.

If the timescale for frictional spindown, T_f, is smaller than that for buoyancy shutdown, T_b, then the fluid is decelerated before the thermal wind inside the bottom boundary layer acts to reduce the flow near the bottom.

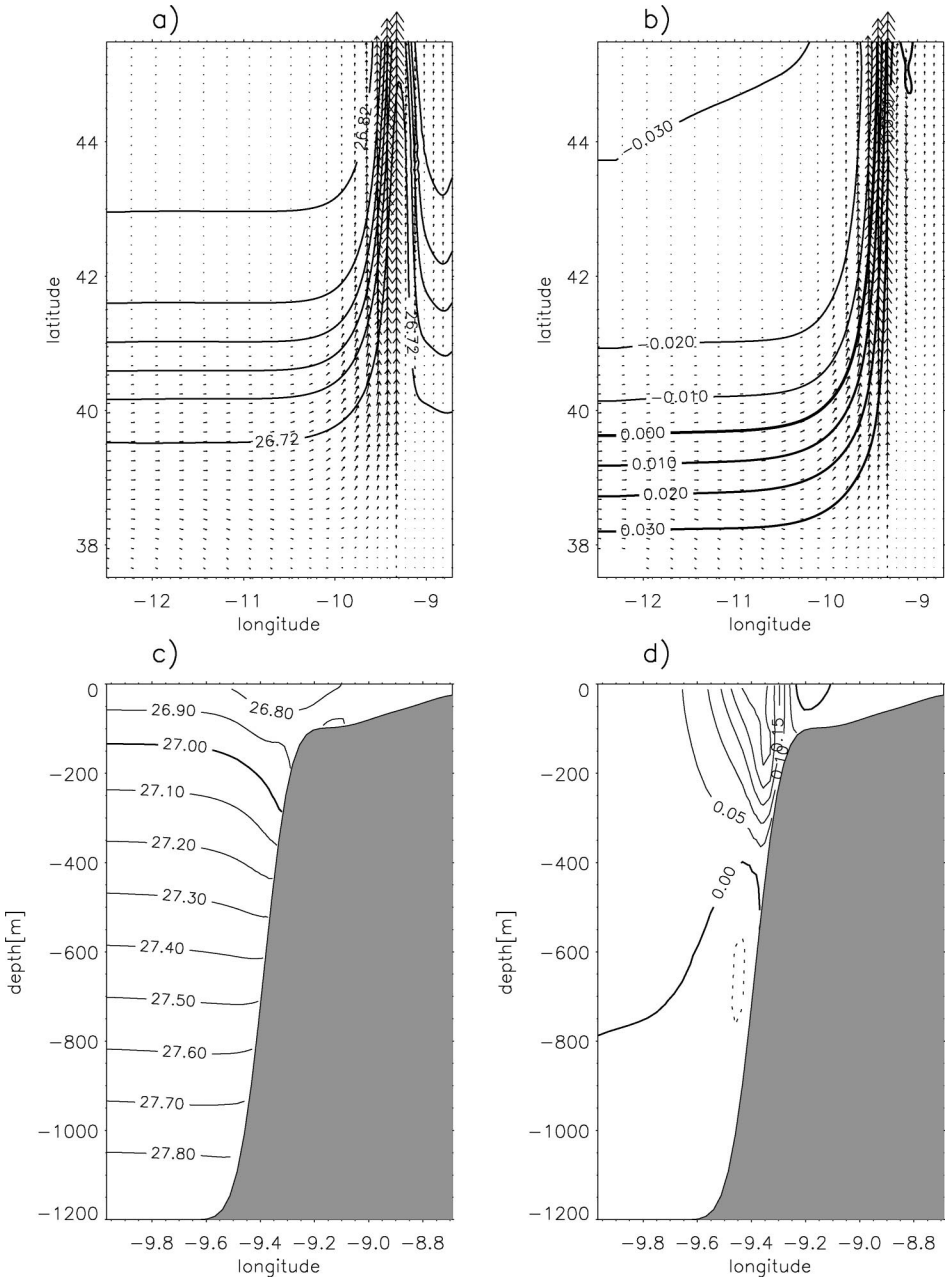

FIG. 4. Horizontal and vertical structure of the adjusted density-driven EPC at the quasi steady state (day 45 of the base run): (a) lines of surface density anomaly and surface velocity vectors plotted with one-fourth of the resolution (maximum vector corresponds to 20 cm s^{-1}), (b) same as (a) but with sea surface anomaly lines (thicker lines correspond to positive anomalies), (c) cross-slope section of density anomaly, and (d) cross-slope section of alongshore velocity (lines represent increments of 0.05 m s^{-1}). Dotted lines correspond to negative (equatorward) velocities.

Taking representative values for the slope zone of $\alpha = 0.05$, $r = 3 \times 10^{-4}$ m s^{-1}, $U = 0.2$ m s^{-1}, $f = 10^{-4}$ s^{-1}, $N = 3 \times 10^{-3}$ s^{-1}, and $H = 300$ m, we estimate $T_f = 12$ days and $T_b = 1$ day. For the shelf with $\alpha = 0.002$, $H = 80$ m, and $U = 0.1$ m s^{-1}, the estimates are quite different: $T_f = 3$ days and T_b is on the order of several years.

Over the slope, T_f is much larger than T_b, suggesting a reduction of the effect of friction on the poleward slope flow. At this cross-shelf position, the current may become persistent and significant at large distances downstream of the generation zone as seen in the models of Chapman and Lentz (1997). In the shallow shelf zone, the buoyancy shutdown timescale is too long in com-

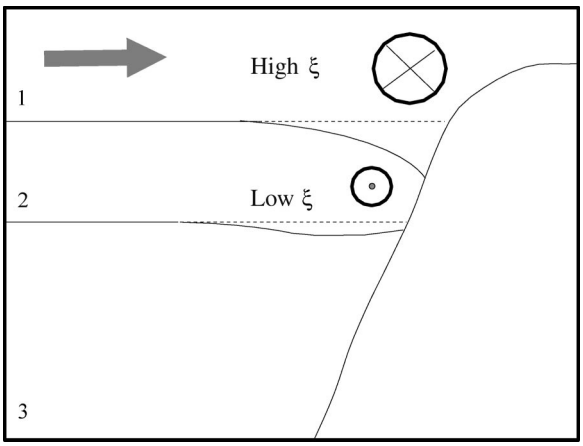

FIG. 5. A conceptual three-layer system illustrating the adjustment of an onshore flow impinging on the slope.

parison with the time for frictional spindown; $T_b \gg T_f$, and all the unforced flow strongly decays in just a few days (Chapman 2002). The location of the poleward flow over the slope is therefore associated with a minimum in the action of bottom friction.

4. Comparison of the simulated EPC with observations

Figure 1 shows a surface temperature distribution off the western Iberian Peninsula taken in February 1998 (Fig. 1a) and a cross-slope section of density anomaly taken in the beginning of February 2000 (Fig. 1b). (Unfortunately, density observations from February 1998 are sparse and shallow, and the vertical structure close to the slope is not well resolved.) In Fig. 1, the observed EPC is seen to replicate three characteristics of the modeled poleward flow. In Fig. 1a, the poleward warm tongue is evident, with a width of about 50 km, separated from the coast by colder waters and narrowing in the northward direction. In Fig. 1b the vertical structure is well resolved and it is possible to observe the presence of the tongue and the bending of the isopycnals in the upper 500 m. The isopycnals downwell against the slope by about 150 m (e.g., the 27.1 isopycnal). At deeper levels, the isopycnals tend to be flat or tilted slightly upward. The width of the tongue structure in Fig. 1b is about 35–40 km. Similar patterns are found in Frouin et al. (1990).

The general characteristics of the simulated EPC are present in other EPC systems as well. The Davidson Current is also surface-intensified and has an associated equatorward undercurrent (Hickey 1998). Measurements taken in central California (Noble and Ramp 2000) show a significant surface intensification of the poleward flow in that zone. Considerable observational evidence in agreement with the simulated EPC may be found for the Leeuwin Current (e.g., Smith et al. 1991). In this EPC, all major characteristics are particularly clear, especially the vertical structure of the current and the presence of the undercurrent, which in some cases has magnitudes as high as 15 cm s^{-1}.

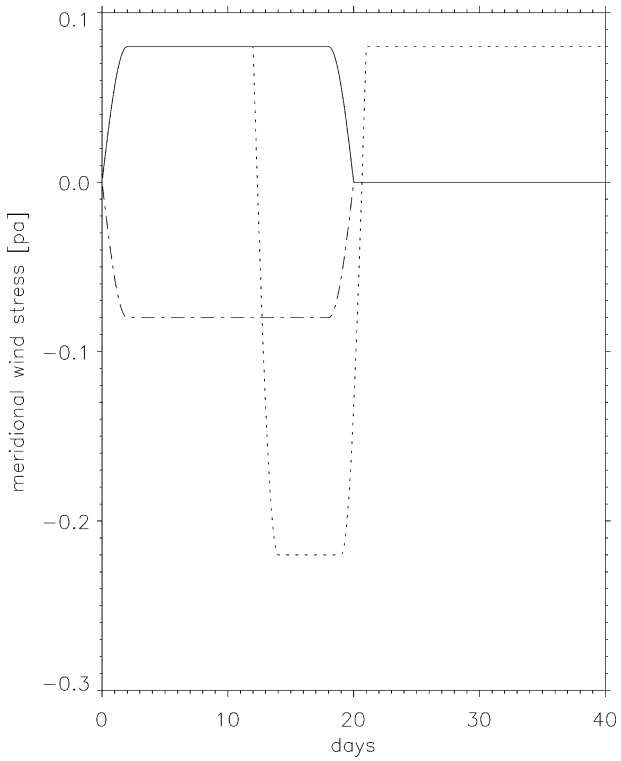

FIG. 6. Time evolution of the meridional wind stress applied in the wind-forced simulations: downwelling (solid), upwelling (dash–dotted), and reversal with intense upwelling pulse (dotted).

5. Wind forcing

The central purpose of the work is the investigation of the response of the quasi-steady-state EPC analyzed above to wind forcing. The experiments concentrate on week-to-month-scale wind events as represented in Fig. 6. Three different situations are considered. In the downwelling-favorable case, a constant northward wind of 0.08 Pa acts during a period of 20 days (one-half of the simulation time) after which the wind is relaxed and the density field readjusts with no atmospheric forcing during the next 20 days. The second event is the same except that the wind stress has the opposite sign to simulate an upwelling situation. Third, we examine a strong reversal of the meridional component of wind stress by introducing into a moderate downwelling-favorable event a week-scale intense upwelling-favorable pulse (0.2 Pa, corresponding to a wind of about 10 m s^{-1}). The applied stress is horizontally uniform in all the cases.

a. Response to a downwelling-favorable wind event

The applied surface wind stress is positive for 20 days, ramping smoothly from zero to a constant value

of 0.08 Pa within the first two days and decreasing to zero at the end of the forcing period. After that, the stress is zero during the second half of the simulation (Fig. 6). The results presented below have been averaged over an inertial period. Hourly plots at different locations (not shown) reveal that superinertial variability is not important.

The response of the surface fields to positive wind stress is presented in Fig. 7. The results correspond to day 0 (the initial quasi steady state of Fig. 4), day 15 (during the downwelling event), and day 32 (12 days after wind relaxation). The area of the plots corresponds to the dashed box of Fig. 2.

At the outer slope, the free surface is not significantly affected by the wind event. However, sea surface height over the shelf increases quickly and by day 4 (not shown) does not show significant differences to the corresponding field of day 15 (Fig. 7c). Once the wind event has ceased, the free surface relaxes to values similar to those of the initial state with the exception of a cross-slope gradient that is somewhat weaker (Figs. 7a, e).

The surface velocity (vectors in the right column of Fig. 7) responds at the very beginning (not shown) with a small increase of northward velocity over all the domain. After that, however, the response within the shelf and slope zones differ. Significant enhancement in the poleward flow is noticed only shoreward of the 150-m isobath where maximum velocities up to 25 cm s^{-1} are observed within the inner shelf. (Velocity magnitudes are clearer in the cross-shore transects provided below.) Over the slope zone, the largest change is in the coastward component associated with onshore Ekman transport (Fig. 7d). In contrast to the shelf zone, here the poleward current is weaker.

The alongshore flow over the shelf responds quickly to the shutdown of the wind stress (Fig. 7f) but the decrease of the flow magnitude over the slope continues beyond the wind event and by day 32, the maximum of the slope flow is about 20 cm s^{-1}.

As a result of coastal convergence, the surface density tongue is advected shoreward (Fig. 7d) and its inner side, while partially eroded by vertical homogenization (discussed below), is incorporated in the northward wind-driven flow. After the wind has stopped, a second tongue starts to develop (Fig. 7f) in response to changes in the relative position of the density and velocity fields over the slope. Within the initial quasi steady state (day 0), these fields are almost parallel and the advection of density ($\mathbf{u} \cdot \nabla \rho$) is not significant. However, as the tongue is advected shoreward, the isopycnals cross the poleward flow and the term $\mathbf{u} \cdot \nabla \rho$ becomes important leading to alongshore buoyancy transport and to the generation of the second tongue (see density anomaly in Fig. 7f).

The integrated transport crossing the standard section northward at the initial state is 1.2 Sv. During active downwelling-favorable wind (day 15), this value is 0.3 Sv higher. This enhanced transport arises from an increased (0.55 Sv) transport on the shelf and despite a reduction in transport (0.25 Sv) within the slope zone. After the relaxation of the wind (day 32), this transport deficit of 0.25 Sv in the poleward slopeflow is maintained. This permanent decrease in the density-driven slope-current transport is related to modifications in the initial gradient of the free surface and in the baroclinic structure of the tongue (see below).

The response of the cross-shore structure of the poleward flow to the downwelling wind event is presented in Fig. 8. The alongshore component of the flow at the slope is not strongly modified under the action of the positive wind stress (cf. Figs. 8d and 8b). The effects of the wind forcing on the slope current become important after the event (day 32) when the poleward flow is slightly broader and weaker with a maximum of about 20 cm s^{-1} in the alongshore component (Fig. 8f).

As the Ekman transport spins up, the surface low-density tongue is advected shoreward (Fig. 8c) within the surface boundary layer. For the offshore side of the tongue, the stratification is relatively weak and by density overturning a mixed layer of about 60-m depth develops with a consequent decrease of the horizontal cross-slope density gradients. This partially modifies the initial thermal wind equilibrium between density and velocity fields at the slope and contributes to the reduction of the transport of the density-driven current. On the inshore side of the tongue, the stratification is larger due to the onshore advection of density and thinning of the surface boundary layer. The latter is observable in the cross-shore component for day 15 in Fig. 9. In the same place, the isopycnals dome, indicating that only the near surface part of the tongue is being transported onto the shelf (Fig. 8c). Inshore of this point, the vertical mixing induced by the bottom layer homogenizes the water column and a density front is generated.

The lighter water that is filling the inner shelf moves under the heavier shelf water because of Ekman transport within the bottom boundary layer, leading to convective mixing and thickening of the layer (e.g., Trowbridge and Lentz 1991; Gawarkiewicz and Chapman 1992). Although this mechanism promotes an interaction with the interior flow by the thermal wind inside the bottom boundary layer (e.g., Chapman 2002), the consequences are not significant, as will be seen later in the comparison with the wind-forced experiment without density tongue.

In the course of the downwelling event, a ''laid s''-shaped front is generated at the upper slope and outer shelf. This baroclinic structure is responsible for some weak shelf circulation observed by day 32 (Figs. 8e, f). Over the outer shelf, $\partial\rho/\partial x$ is positive and is in geostrophic equilibrium with a southward baroclinic flow of just a few centimeters per second. At midshelf, the water column is almost homogeneous and a baroclinic northward flow close to 5 cm s^{-1} is observed in thermal

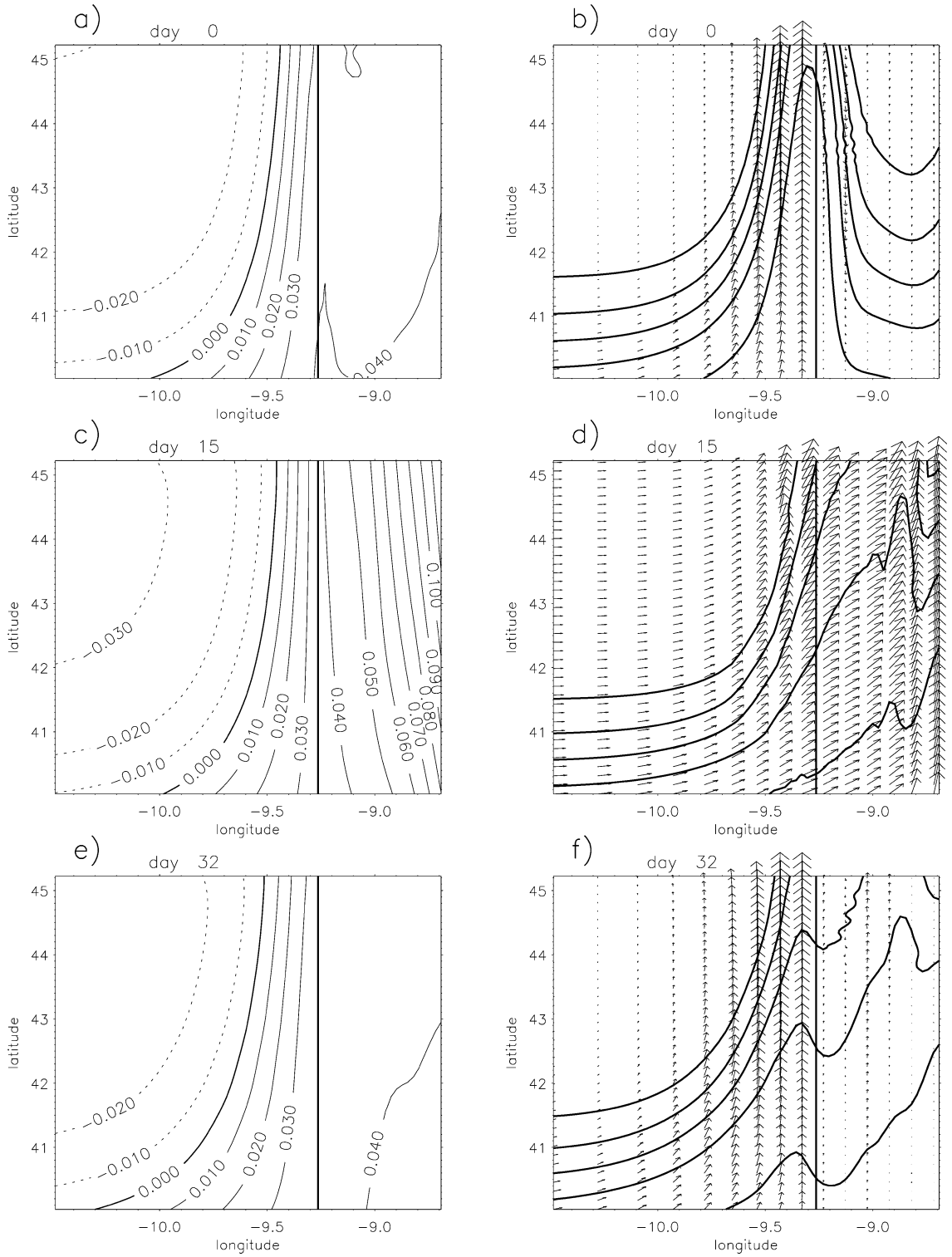

FIG. 7. Horizontal field plots for the downwelling experiment at days 0, 15, and 32. (a), (c), (e) The sea surface height anomaly (m) is with dashed lines corresponding to low (negative) anomalies. (b), (d), (f) The surface density anomaly (plotted every 0.02 kg m^{-3}). Vectors represent the surface velocity plotted with one-fourth of the grid resolution (the largest vector corresponds to 0.30 m s^{-1}). The *x* axis is exaggerated for clarity and the thicker line represents the 150-m isobath.

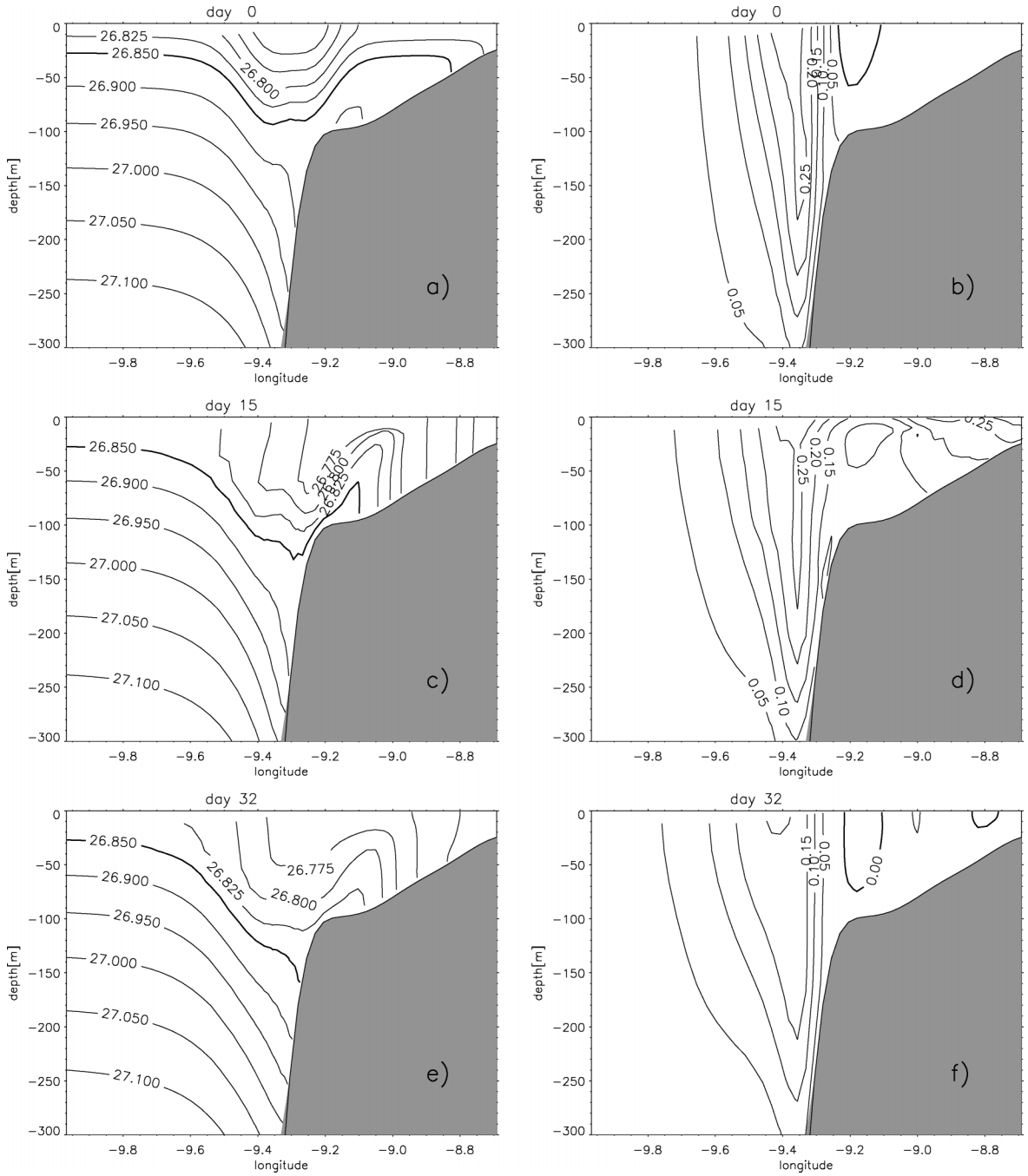

FIG. 8. Cross-slope sections for the downwelling experiment at days 0, 15, and 32. (a), (c), (e) The density anomaly (kg m^{-3}). (b), (d), (f) The alongshore velocity component plotted every 0.05 m s^{-1}. Solid lines correspond to positive (northward) values and the thicker line corresponds to 0.

wind equilibrium with the density gradient (see Fig. 8f and the middle shelf in Fig. 7f).

In order to compare these results with the response of the slope/shelf system to a downwelling event in the absence of the slope-poleward flow, a parallel experiment with no initial velocity and stratification independent of the horizontal dimensions—that is, no poleward flow—was conducted. The initial fields are therefore

$$\sigma(z) = 26.9 - \frac{0.86z}{1000}, \tag{4}$$

and the wind forcing is the same as described above.

The redistribution of the density over the shelf in the absence of the EPC (Fig. 10) is no different from what has been observed in similar studies (e.g., Middleton and Cirano 1999). As surface lighter water is advected

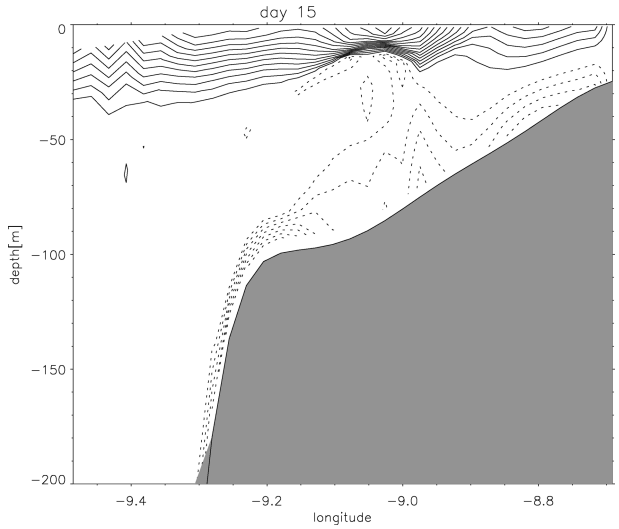

FIG. 9. Cross-slope section of cross-shore velocity component at day 15 for the downwelling experiment. Lines are plotted every 0.5 cm s^{-1} and dashed lines correspond to negative (offshore) values.

coastward within the surface boundary layer, the inner shelf is vertically homogenized and the northward flow is essentially barotropic. Along the bottom, cross-isobath buoyancy flux is induced by the bottom Ekman transport and the density overturning increases the thickness of the boundary layer.

The structure and magnitude of the shelf flow is not very different from the preceding experiment with EPC. In the case of no poleward current, the northward flow decays rapidly at the shelf break, but within the inner shelf the velocity values are similar. The wind-driven flow at the slope is not significant. The horizontal scale of downwelling of the isopycnals at the slope in this experiment is about 15 km, while in the experiment with the density-driven poleward current it is about twice this value. The similarities of the shelf flow in both experiments suggests that the shelf responds to the positive wind stress quasi independently of the density-driven current along the slope.

In the bottom layer, however, some differences to the preceding experiment may be discovered. In particular, at the shelf break, the transport within the bottom layer is different in the two experiments. For the case with no initial poleward current at the slope, the cross-shelf velocity decays past the shelf break (Fig. 10c) indicating a possible detachment of the bottom boundary layer as

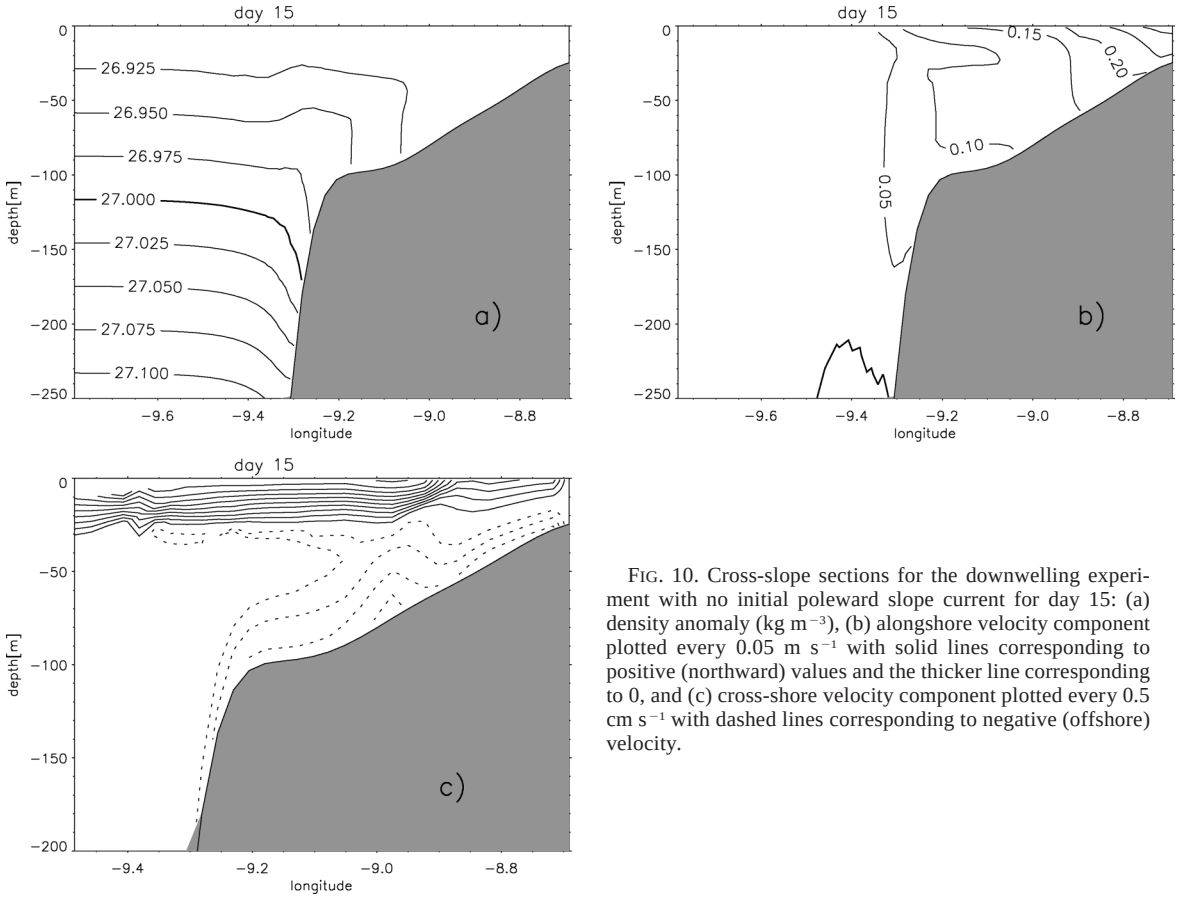

FIG. 10. Cross-slope sections for the downwelling experiment with no initial poleward slope current for day 15: (a) density anomaly (kg m^{-3}), (b) alongshore velocity component plotted every 0.05 m s^{-1} with solid lines corresponding to positive (northward) values and the thicker line corresponding to 0, and (c) cross-shore velocity component plotted every 0.5 cm s^{-1} with dashed lines corresponding to negative (offshore) velocity.

discovered in experiments with similar characteristics (Gawarkievicz and Chapman 1992). In the case with the density-driven flow along the slope, the cross-isobath component in the bottom boundary layer is reinforced at the shelf break and the flow penetrates downslope to deeper levels (Figs. 9 and 10c). Thus, the presence of the poleward current has the effect of extending the bottom boundary layer from the shelf onto the slope, increasing the cross-isobath transport of shelf waters.

b. Response to an upwelling-favorable wind event

The wind stress used to force the ocean in this case has exactly the same characteristics as the one used in the preceding section except that it is directed oppositely.

The response of the surface fields to negative wind stress is presented in Fig. 11. The surface fields correspond to the small box of Fig. 2. Off the slope, the free surface is not significantly affected by the wind event. Sea surface height over the shelf decreases during the first days, and by day 4 (not shown) does not show significant differences from the corresponding field of day 15 (Fig. 11c), indicating that at this time the southward flow is already balancing the free surface tilt. Over the shelf, the free surface anomaly field is characterized by a depression that is intensified to the north.

The velocity field is equatorward (negative) with magnitudes in excess of 15 cm s^{-1} and a maximum of 30 cm s^{-1} within the inner shelf (Fig. 11d). A decrease of about 5 cm s^{-1} is noticeable in the poleward current at the slope. The surface density field evolution (right column in Fig. 11) is characterized by a broadening of the light water tongue and the development of a band of denser upwelled water over the shelf.

After the shutdown of the wind stress (day 20), the surface signature of the poleward current, initially aligned along the slope, has shifted offshore. Close to the shelf break, the flow is poleward, crossing the isopycnals (Fig. 11f), and the term $(\mathbf{u} \cdot \nabla\rho)$ is again significant leading to density advection along the upper slope and to the broadening of the tongue. This density advection increases the cross-slope density contrast. Shoreward of the shelf edge, the flow is southward and transports denser upwelled water. At the upper slope, the flow is northward and transports lighter water (Figs. 11d,f). With the strengthening of the shelfbreak front, surface instabilities develop (Fig. 11f) and grow throughout the simulation.

The wavelength of the instabilities is about 25 km. They appear to be trapped to the front and do not propagate meridionally. The possibility that these instabilities have a barotropic origin can be tested by calculating the cross-current gradient of the potential vorticity,

$$P = \left(f - \frac{\partial \mathbf{v}}{\partial x} \right) \Big/ h, \tag{5}$$

where f is the Coriolis parameter, $\mathbf{v}$ is the depth-integrated along-slope velocity, and h is the local depth. Shear instabilities may develop if the cross-current derivative of P changes its sign. However, here we find that the cross-shore gradient of P has only an almost negligible reversal.

This result suggests that the baroclinic structure of the shelf front may play a role in the instabilities. The internal Rossby radius in the present experiment is rather small over the shelf. Taking the Coriolis parameter $f = 10^{-4}$ s^{-1}, the depth at the outer shelf $h = 100$ m, and the buoyancy frequency at the time of the unstable event $N = 0.0038$ s^{-1}, an estimate for the Rossby radius $R = Nh/f$ is about 3.8 km. Considering a reference scale for the baroclinic instability of $2\pi R$, the wavelength would be approximately 24 km, which is coincident with the scale of the instabilities that are observed. The instabilities do not grow sufficiently to perturb the slope flow, however.

Computation of the integrated transport along the standard section reveals that during the wind event the transport over the shelf is approximately the same as that over the slope, but in the opposite direction. After the wind event, the slope transport has been reduced from 1.2 to about 0.9 Sv, approximately the same reduction as that for the downwelling experiment. The evolution of the cross-slope structure of the density and alongshore velocity in response to the upwelling event is presented in Fig. 12. Although the intensity of the flow decreases by about 5–10 cm s^{-1} during and after the upwelling episode, the general structure of the density-driven poleward slope current is not strongly affected.

As the tongue moves offshore within the surface boundary layer, a homogenization of the outer shelf occurs due to mixing of the inshore side of the tongue (see Figs. 12a,c). Consequently, the shelf edge counterflow decreases and is incorporated within the wind-driven current. By day 15, (Fig. 12d) the alongshore velocity inside the shelf is southward everywhere with values above 10 cm s^{-1}, increasing to 30 cm s^{-1} near the coast.

While the surface boundary layer has approximately the same depth both over the shelf and offshore, indicating a uniform offshore transport (Fig. 13), the return flow through the bottom boundary layer diminishes at the shelf break. This occurs because seaward of the shelf edge, the along-isobath flow changes from southward to northward, reducing the coastward cross-isobath Ekman transport. Consequently, the return flow is obtained from shallower levels, and no significant cross-slope density flux is produced resulting in a weakly stratified bottom layer (see Figs. 12c,e).

After the relaxation of the wind, the initial structure of the tongue over the slope begins to recover (Fig. 12e) because of the restoration of the poleward advection of density. As the inshore branch of the tongue penetrates

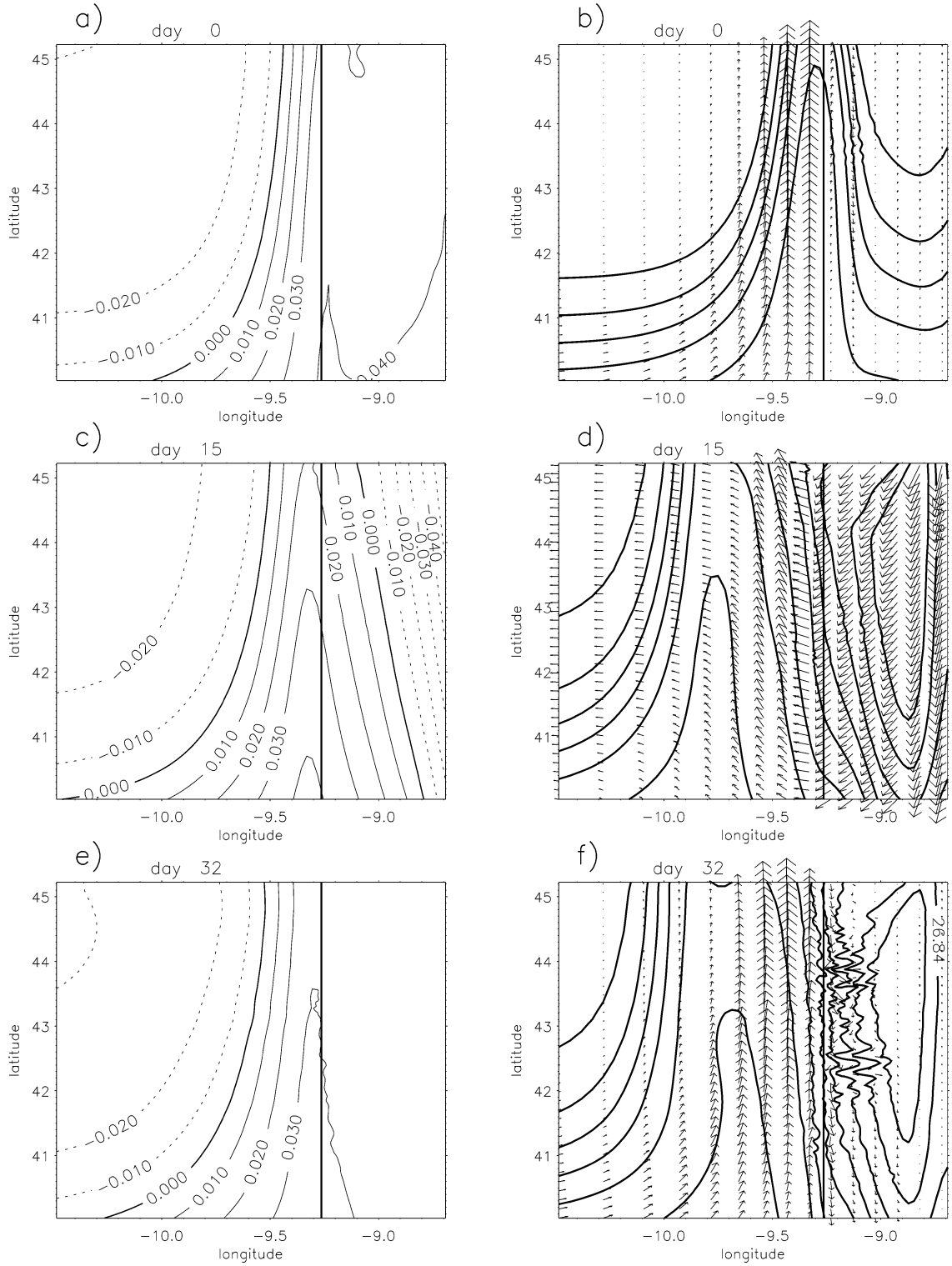

FIG. 11. Horizontal field plots for the upwelling experiment at days 0, 15, and 32. (a), (c), (e) The sea surface height anomaly (m) is shown, with the dashed lines corresponding to low (negative) anomalies. (b), (d), (f) The surface density anomaly plotted every 0.02 (kg m^{-3}). Vectors represent the surface velocity plotted with one-fourth of the grid resolution (the longest vector corresponds to negative 0.3 m s^{-1}). The *x* axis is exaggerated for clarity, and the thicker line represents the 150-m isobath.

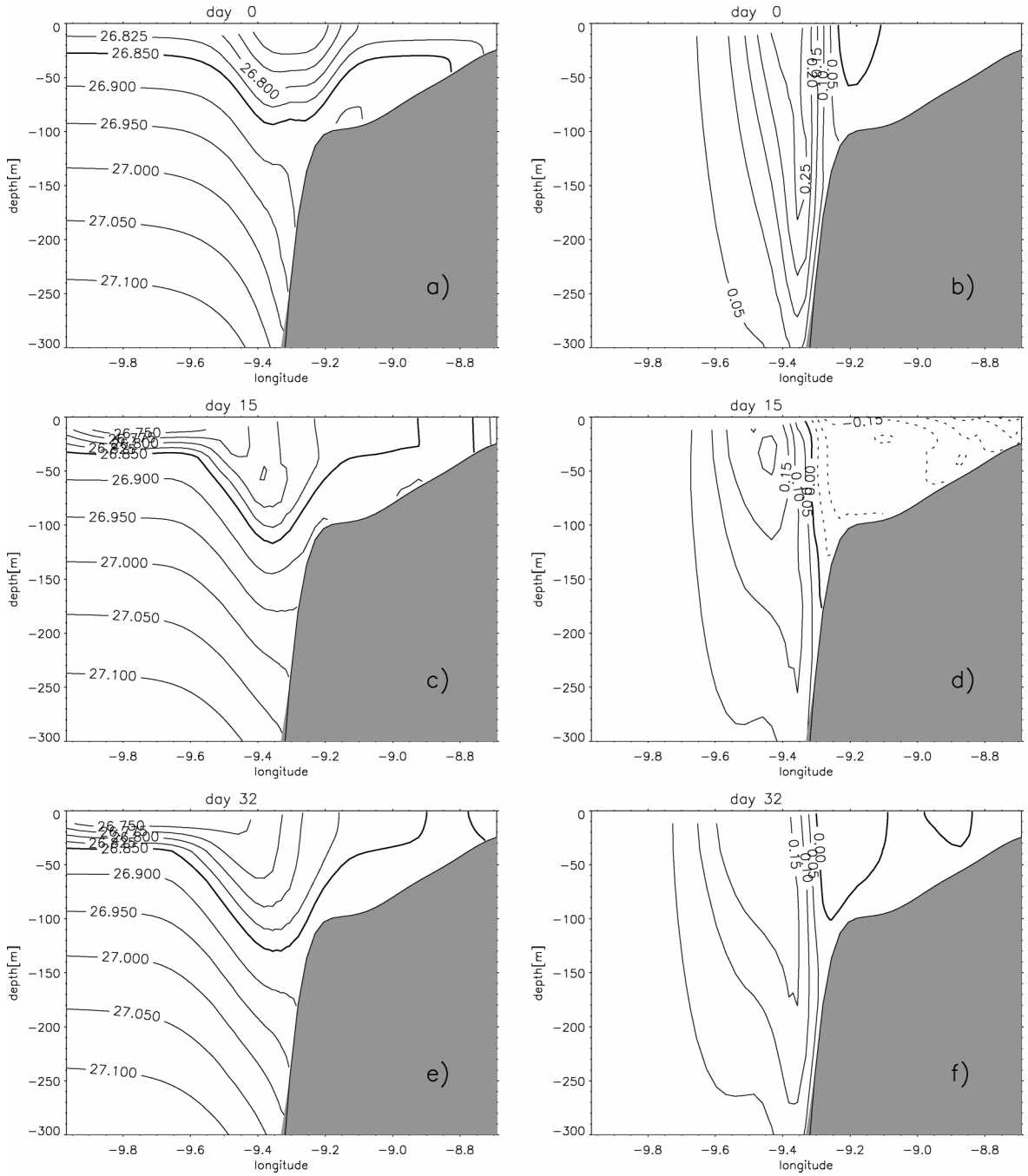

FIG. 12. Cross-slope sections for the upwelling experiment at days 0, 15, and 32. (a), (c), (e) The density anomaly (kg m^{-3}). (b), (d), (f) The alongshore velocity component plotted every 0.05 m s^{-1}. Solid lines correspond to positive (northward) values and dashed to negative (southward). The thicker line corresponds to 0.

the outer shelf, the weak counterflow associated with it reappears at the shelf break (see Figs. 12b,f).

An experiment aimed at the response of the shelf/slope system in the case of no density-driven slope current was also conducted. The wind forcing is exactly the same and the initial density field is calculated using the expression (4). The cross-shore structure of the alongshore velocity component and density for the standard section is represented in Fig. 14. The flow is quasi barotropic and oriented southward extending beyond the shelf break. Velocities of about 5 cm s^{-1} are observed over the upper slope and above 10 cm s^{-1} on the outer shelf.

Generally, the magnitude of the southward currents

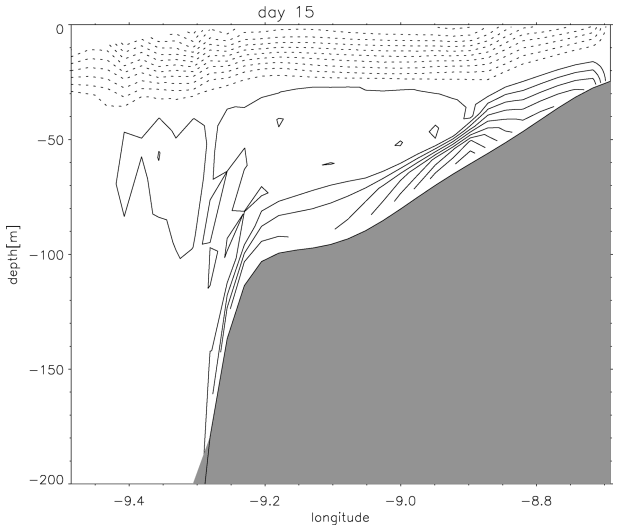

FIG. 13. Cross-slope section of cross-shore velocity component at day 15 for the upwelling experiment. Lines are plotted every 0.5 cm s^{-1} and dashed lines correspond to negative (offshore) values.

over the shelf are similar in both experiments. At the upper slope, the main difference is the greater offshore extension and depth penetration of the southward flow in the case of no density-driven poleward current (see Figs. 12d and 14b). The rapid recovery of northward flow along the upper slope in the case of the experiment with density-driven poleward current also contrasts with the weak southward baroclinic current that remains in the case of no poleward flow for longer times after the upwelling event (not shown).

An important difference between both experiments is the cross-isobath transport within the bottom boundary layer (see Figs. 13 and 14c), and the associated cross-isobath buoyancy flux. In the case of no density-driven flow along the slope, the transport of denser water upslope introduces stratification inside the bottom boundary layer (Fig. 14a). In the case of upwelling with density-driven poleward slope flow, the inshore bottom Ekman transport is reduced at the shelf break and no significant increase in the bottom density is observed, because the return flow originates at shallower levels.

c. *Response to a reversal of wind stress*

A week-duration intense upwelling-favorable pulse in the middle of a moderate downwelling period simulates

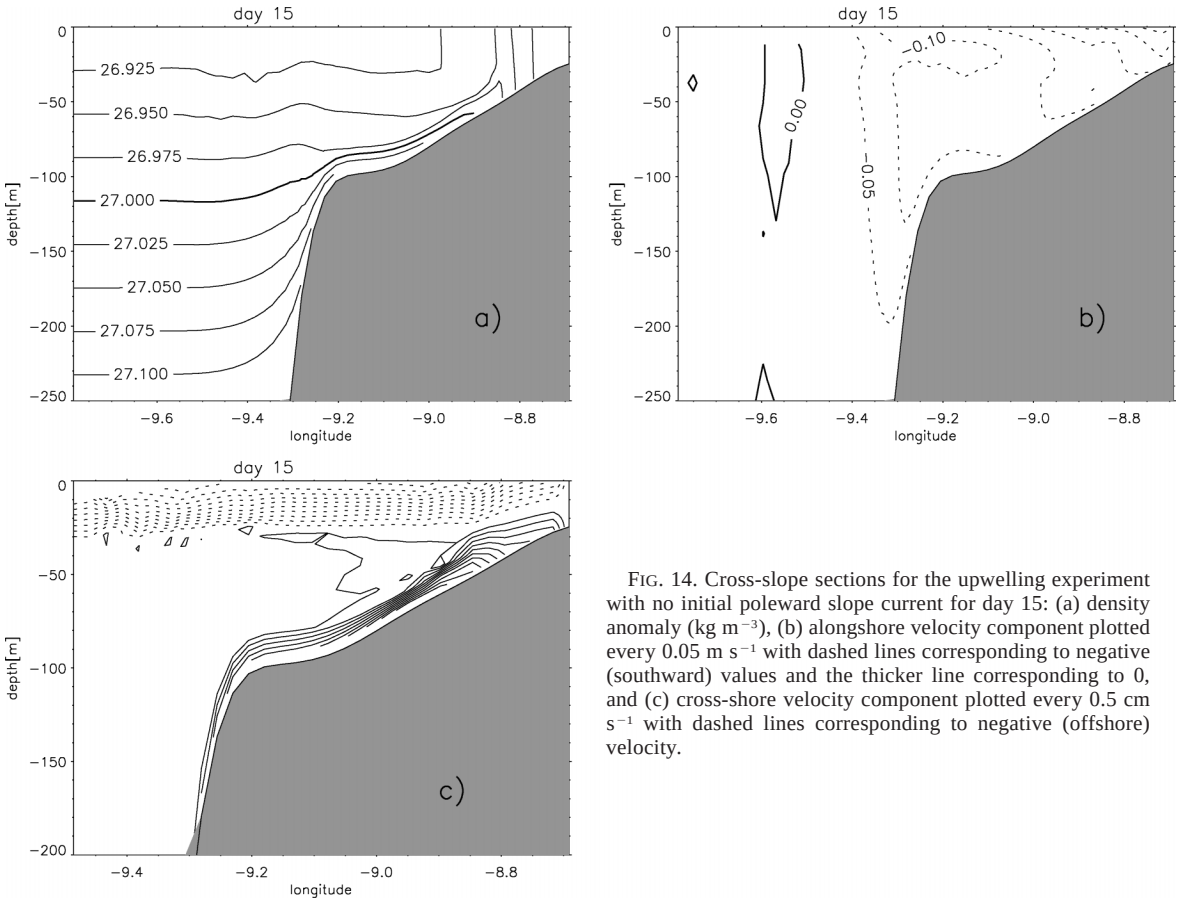

FIG. 14. Cross-slope sections for the upwelling experiment with no initial poleward slope current for day 15: (a) density anomaly (kg m^{-3}), (b) alongshore velocity component plotted every 0.05 m s^{-1} with dashed lines corresponding to negative (southward) values and the thicker line corresponding to 0, and (c) cross-shore velocity component plotted every 0.5 cm s^{-1} with dashed lines corresponding to negative (offshore) velocity.

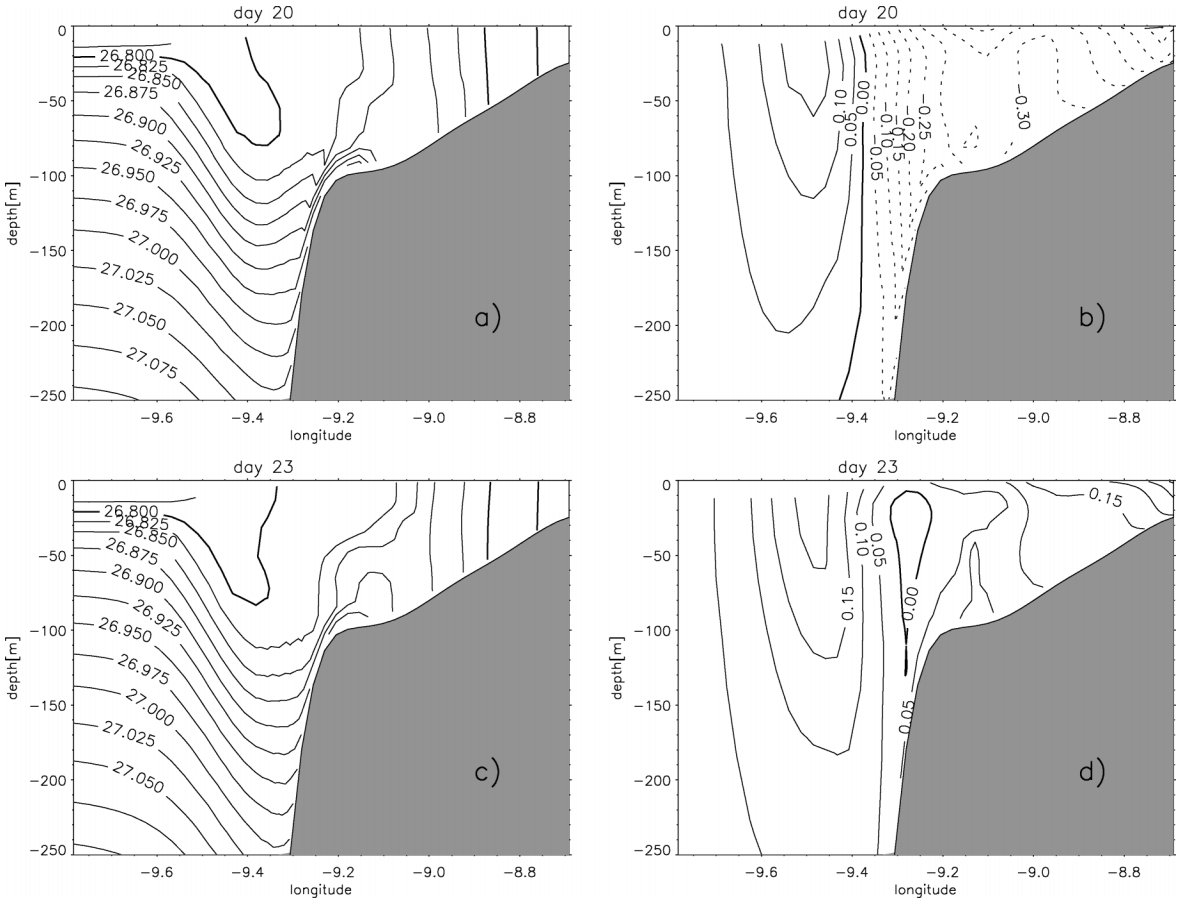

FIG. 15. Cross-slope sections for days 20 and 23 of the experiment with a week-long upwelling event: (a) and (c) density anomaly (kg m^{-3}); (b) and (d) alongshore velocity component plotted every 0.05 m s^{-1} with dashed lines corresponding to negative (southward) velocity and solid to positive (northward).

the effect of a marked reversal in the meridional wind component. This type of wind forcing is typical of winter and early spring upwelling episodes off western Iberia. The motivation is to test the robustness and stability of the slope-poleward flow to strong upwelling events.

Stronger barotropic currents and strong vertical homogenization are observed over the shelf (Fig. 15) and the southward flow extends farther offshore from the shelf break than in the preceding experiments. A particular difference from the ''steady'' upwelling experiment (Fig. 12) is that there is a separation of the poleward flow from the upper slope. The southward undercurrent merges at the upper slope with the shelf upwelling flow (see Fig. 15b). This connection, noticeable by day 20, causes significant upslope transport within the bottom boundary layer (note the accumulation of denser water at the shelf edge in Fig. 15a) that corresponds to shoreward cross-isobath velocities up to 10 cm s^{-1}.

We would speculate that this separation of the poleward flow could be the motivation for loss of bathymetric control of the current and preconditioning for the further development of instabilities. This effect, however, does not last long and the poleward flow does reattach to the shelf as well as intensifies as soon as the wind reverses. Three days later, the poleward flow system is completely reestablished. No sign of unstable modes were detected through the end of the simulation. As studied in Haidvogel et al. (1991), poleward flows are much more stable than equatorward ones. The development of instabilities within eastern poleward currents is thus more likely to be related to the presence of bathymetric irregularities that contribute to the separation of the flow (e.g., Peliz et al. 2003). Wind events alone are unlikely to be responsible for the development of unstable structures along the poleward flows as hypothesized by Thomson and Gower (1998). Indeed, in all the experiments conducted during this investigation the only signs of instability were associated with the shelf edge front during the upwelling event.

6. Parameter variation

Because of the importance of the bottom boundary layer in the present experiments, it was decided to focus the sensitivity tests on the bottom drag parameterization

and on the vertical mixing scheme. Parallel simulations with the Mellor–Yamada level 2.5 (MY25) closure model were performed for both upwelling and downwelling experiments. It was observed that the general features of simulations with the MY25 mixing were not different except on the inner shelf. With the Large et al. (1994) vertical mixing scheme, the homogenization of the shallow zones due to the connection of the surface and bottom boundary layers starts at larger depths leaving a narrow band of different density attached to the coast (see an example in Figs. 12c and 14a). This feature is absent from the simulations with the MY25, where the divergence of the Ekman layers is only observed very close to the coast. Nevertheless, this difference in the inner shelf dynamics does not affect in any way the circulation within the slope zone.

The experiments with varying bottom drag intensities were performed for the upwelling case. The simulations utilized one-third (10^{-4} m s^{-1}) and double (6.0×10^{-4} m s^{-1}) the base value. The experiments revealed that the shelf current intensities increase/decrease, but no significant differences were noted in the poleward slope current. This is in keeping with the discussion, above, that bottom-dissipative timescales are long in the slope zone for the parameter values studied here.

7. Discussion and conclusions

The primary responses of the density-driven slope-poleward flow to wind forcing are (i) a decrease of the cross-shelf gradient of the free surface at the shelf break and, consequently, a decrease of the barotropic alongslope flow and (ii) modifications in the thermal wind equilibrium of the poleward current by the redistribution of density in the low-density tongue. The density modifications are forced by Ekman transport and vertical mixing. Also, (iii) the adjustment of the new density field includes advection of density, in contrast with the situation of the initial quasi steady state wherein both density and velocity fields are parallel.

Both upwelling and downwelling wind events contribute to a decrease in transport of the poleward density-driven flow by 0.2–0.3 Sv (from 1.2 Sv). Downwelling events tend to concentrate the density tongue toward the coast where it is partially mixed, contributing to significant buoyancy input onto the shelf and to the generation of weak fronts that will be balanced by some residual circulation along the shelf. In the slope zone, a secondary tongue structure is developed after the event. Upwelling events tend to spread the density tongue offshore, but, because of the continuous advection of lighter waters northward along its shore edge, the density tongue gets broader. The continuous northward advection of southern lighter water along the slope reinforces the generation of upwelling fronts.

There is no evidence in the present experiments that the poleward density-driven flow can become an undercurrent under the action of upwelling favorable winds. The intensity of the current diminishes and its core at the surface moves offshore by some kilometers. Beyond this, the vertical structure of the velocity field is not strongly affected by the event.

Downwelling events do not intensify the poleward flow over the slope. Rather, a decrease in the velocity is noticeable, although the vertical structure of the current is not significantly modified by the event.

Wind forcing acts to modulate the poleward density-driven flow by modifying its intensity and position relative to the shelf break. At week-to-month time scales, wind events do not introduce strong changes in the poleward slope currents. These results are robust even with intensified upwelling episodes. In none of the experiments has the poleward flow developed unstable fluctuations in response to wind forcing.

The comparison of the shelf/slope response with and without a density-driven EPC to wind forcing indicates that these processes may have a considerable degree of independence and that the response is apparently linear. Wind-driven currents are basically limited to the shelf while density-driven flow is arrested at the slope.

Significant differences were observed within the bottom boundary layer. The presence of the poleward flow at the slope constitutes an important constraint on bottom layer dynamics. In the case of downwelling, it acts to provide continuity to the cross-isobath flow at the shelf break; in consequence, shelf waters reach deeper levels downslope. In the case of upwelling, the poleward current disrupts that continuity at the shelf break and consequently the return flow comes from shallower levels.

Some observational confirmation of the findings presented here is provided in Noble and Ramp (2000). The authors describe a yearlong set of current observations across the slope in central California off San Francisco. A modal decomposition of the alongshore component is calculated and the cross-slope structure of the modes is analyzed. The first mode shows the dominant surface-intensified coherent (alongshore) current corresponding to the 40-km-wide poleward slope flow. A second mode, strongly correlated with local wind stress fluctuations (3–16 days) was observed to be consequential off the shelf break to distances up to about two Rossby radii. It is shown that the first mode corresponds to the low-frequency surface-intensified slope-current with magnitudes above the time-averaged currents, indicating that the high-frequency fluctuations (mode 2) acts to decrease the mode-1 intensity. Besides the structure of their mode 1 (which bears resemblance to the present simulated EPC), other interesting aspects for the present analysis are two unexpected characteristics of mode 2: its offshore extent and its surface intensification. (Mode 2 is influential only in the upper 300 m and it is vertically sheared.)

In our opinion, the mode 2 of Noble and Ramp (2000) observations might be associated with changes in the baroclinic structure of the poleward flow through den-

sity redistribution forced by the surface wind stress as analyzed in section 5. This effect would explain the offshore extension of the wind-driven variability as well as the vertical structure of the fluctuations.

Other evidence of the interaction between wind and density-driven slope-flow are presented for the Leeuwin Current by Smith et al. (1991). The authors show time averages of the alongshore flow for periods with different wind types. They show that the the surface slope flow is stronger in the period of weak and variable wind (March–May). During the period of steady-upwelling wind (November–January), it is weaker, and it is also weaker during the period of variable or poleward-intensified winds (May–July; see their Figs. 2 and 5).

For the IPC system, long series of current measurements resolving the cross-slope structure are, unfortunately, nonexistent. However, to the authors' knowledge, in all reported wintertime observations off western Iberia, the slope-poleward flow is present despite the dominant wind direction (e.g., Santos et al. 2002, manuscript submitted to *Cont. Shelf Res.*).

Acknowledgments. This research was supported by the Portuguese Science Foundation (FCT) under Contract FCT/PRAXIS/P/CTE/11282/98, project SURVIVAL. The first author was partially funded by the Luso-American Foundation during his stay at the Rutgers University. Thanks are given to Hernan Arango for his help with ROMS and to John Wilkin for reading the manuscript. Thanks are also given to one anonymous reviewer and to J. Middleton for all the suggestions and corrections that significantly improved that paper.

REFERENCES

Chapman, D. C., 2002: Decelaration of a finite-width, stratified current over a sloping bottom: frictional spindown or buoyancy shutdown? *J. Phys. Oceanogr.,* **32,** 336–352.

——, and S. J., Lentz, 2002: Adjustment of stratified flow over a sloping bottom. *J. Phys. Oceanogr.,* **27,** 340–356.

Csanady, G. T., 1988: Ocean currents over the continental slope. *Advances in Geophysics,* Vol. 30, Academic Press, 95–203.

Dubert, J., 1998: Dynamique du système de courants vers le pôle au voisinage de la pente continental à l'ouest e au nord de la Péninsule Ibérique. Ph.D. Thesis, University of Bretagne Occidentale, 237 pp.

Frouin, R., A. F. G. Fiúza, I. Ambar, and T. J. Boyd, 1990: Observations of a poleward surface current off the coast of Portugal and Spain during winter. *J. Geophys. Res.,* **95,** 679–691.

Garrett, C., P. MacCreary, and P. Rhines, 1993: Boundary mixing and arrested Ekman layers: Rotating stratified flow near a sloping boundary. *Annu. Rev. Fluid Mech.,* **25,** 291–323.

Gawarkiewicz, G., and D. C. Chapman, 1992: The role of stratification in the formation and maintenance of shelf-break fronts. *J. Phys. Oceanogr.,* **22,** 753–772.

Haidvogel, D. B., and A. Beckman, 1999: *Numerical Ocean Circulation Modeling.* Imperial College Press, 318 pp.

——, ——, and K. Hedstrom, 1991: Dynamical simulations of filament formation and evolution in the coastal transition zone. *J. Geophys. Res.,* **96,** 15 017–15 040.

——, H. G. Arango, K. Hedstrom, A. Beckmann, P. Malanotte-Rizzoli, and A. F. Shchepetkin, 2000: Model evaluation experiments in the North Atlantic basin: Simulations in nonlinear terrain-following coordinates. *Dyn. Atmos. Oceans,* **32,** 239–281.

Hickey, B., 1998: Coastal oceanography of the western North America from the tip of Baja California to Vancouver Island. *The Sea,* A. R. Robinson and K. H. Brink, Eds., Vol. 11, Wiley and Sons, 345–393.

Holland, W. R., 1973: Baroclinic and topographic influences on the transport in the western boundary currents. *Geophys. Fluid Dyn.,* **4,** 187–810.

Huthnance, J. M., 1984: Slope currents and ''JEBAR.'' *J. Phys. Oceanogr.,* **14,** 795–810.

Isemer, H. J., and L. Hasse, 1987: *The Bunker Climate Atlas of the North Atlantic Ocean.* Vol. 2, *Air–Sea Interactions,* Springer-Verlag, 252 pp.

Large, W. G., J. C. McWilliams, and S. C. Doney, 1994: Oceanic vertical mixing a review and a model with nonlocal boundary layer parameterization. *Rev. Geophys.,* **32,** 363–403.

Marchesiello, P., B. Barnier, and A. P. de Miranda, 1998: A sigma-coordinate primitive equation model for studying the circulation in the South Atlantic Part II: Meridional transports and seasonal variability. *Deep-Sea Res.,* **45,** 573–608.

Mazé, J. P., M. Arhan, and H. Mercier, 1997: Volume budget of the eastern boundary layer off the Iberian Peninsula. *Deep-Sea Res.,* **44,** 1543–1574.

Mertz, G., and D. G. Wright, 1997: Interpretations of the JEBAR term. *J. Phys. Oceanogr.,* **22,** 301–305.

Middleton, J. F., 2000: Wind-forced upwelling: The role of the surface mixed layer. *J. Phys. Oceanogr.,* **30,** 745–763.

——, and M. Cirano, 1999: Wind-forced downwelling slope currents: A numerical study. *J. Phys. Oceanogr.,* **29,** 1723–1743.

Neshyba, S. J., Ch. N. K. Mooers, R. L. Smith, and R. T. Barber, Eds., 1989: *Poleward Flows along Eastern Ocean Boundaries.* Vol. 34, *Coastal and Estuarine Studies,* Springer-Verlag, 374 pp.

Noble, A. N., and S. R. Ramp, 2000: Subtidal currents over the central California slope: Evidence for offshore veering of the undercurrent and for direct wind-driven slope currents. *Deep-Sea Res.,* **47,** 871–906.

Pedlosky, J., 1974: Longshore currents and the onset of upwelling over bottom slope. *J. Phys. Oceanogr.,* **4,** 310–320.

Peliz, A., J. Dubert, D. Haidvogel, and B. Le Cann, 2003: Generation and unstable evolution of a density-driven eastern poleward current: The Iberian Poleward Current. *J. Geophys. Res.,* in press.

Pingree, R. D., and B. Le Cann, 1989: Celtic and Armorican slope and shelf residual currents. *Progress in Oceanography,* Vol. 23, Pergamon, 303–338.

Slørdal, L. H., and J. W. Weber, 1996: Adjustment to JEBAR forcing in a rotating ocean. *J. Phys. Oceanogr.,* **26,** 657–670.

Song, Y., and D. B. Haidvogel, 1994: A semi-implicit ocean circulation model using a generalized topography following coordinate system. *J. Comput. Phys.,* **115,** 228–244.

Smith, R. L., A. Huyer, J. S. Godfrey, and J. A. Church, 1991: The Leeuwin Current off Western Australia, 1986–1987. *J. Phys. Oceanogr.,* **21,** 323–345.

Thomson, R. E., and J. F. R. Gower, 1998: Basin-scale oceanic event in the Gulf of Alaska. *J. Geophys. Res.,* **103,** 3033–3040.

Thompson, R. O. R. Y., 1987: Continental-shelf-scale model of the Leeuwin Current. *J. Mar. Res.,* **45,** 813–827.

Trowbridge, J. H., and S. J. Lentz, 1991: Asymetric behavior of an oceanic boundary layer above a sloping bottom. *J. Phys. Oceanogr.,* **21,** 1171–1185.

Weaver, A. J., and J. H. Middleton, 1989: On the dynamics of the Leeuwin Current. *J. Phys. Oceanogr.,* **19,** 625–648.